

Alma Mater Studiorum Università di Bologna
Archivio istituzionale della ricerca

Resonant wave energy harvester based on dielectric elastomer generator

This is the final peer-reviewed author's accepted manuscript (postprint) of the following publication:

Published Version:

Moretti, G., Papini, G.P.R., Righi, M., Forehand, D., Ingram, D., Vertechy, R., et al. (2018). Resonant wave energy harvester based on dielectric elastomer generator. SMART MATERIALS AND STRUCTURES, 27(3), 1-14 [10.1088/1361-665X/aaab1e].

Availability:

This version is available at: <https://hdl.handle.net/11585/660276> since: 2019-02-04

Published:

DOI: <http://doi.org/10.1088/1361-665X/aaab1e>

Terms of use:

Some rights reserved. The terms and conditions for the reuse of this version of the manuscript are specified in the publishing policy. For all terms of use and more information see the publisher's website.

This item was downloaded from IRIS Università di Bologna (<https://cris.unibo.it/>).
When citing, please refer to the published version.

(Article begins on next page)

This is the final peer-reviewed accepted manuscript of:

Moretti, G. et al., 2018. Resonant wave energy harvester based on dielectric elastomer generator. *Smart materials and structures*, 27(3), p.35015.

The final published version is available online at:

<https://doi.org/10.1088/1361-665X/aaab1e>

Rights / License:

The terms and conditions for the reuse of this version of the manuscript are specified in the publishing policy. For all terms of use and more information see the publisher's website.

This item was downloaded from IRIS Università di Bologna (<https://cris.unibo.it/>)

When citing, please refer to the published version.

Resonant wave energy harvester based on dielectric elastomer generator

Giacomo Moretti¹, Gastone Pietro Rosati Papini¹, Michele Righi¹, David Forehand²,
David Ingram², Rocco Vertechy³, and Marco Fontana⁴

¹TeCIP Institute, Scuola Superiore Sant'Anna, Pisa, Italy

²Institute for Energy Systems, The University of Edinburgh, UK

³Department of Industrial Engineering, University of Bologna, Italy

⁴Department of Industrial Engineering, University of Trento, Italy

Abstract

Dielectric elastomer generators (DEGs) are a class of capacitive solid-state devices that employ highly stretchable dielectrics and conductors to convert mechanical energy into high-voltage direct-current electricity. Their promising performance in terms of convertible energy and power density has been mostly proven in quasi-static experimental tests with prescribed deformation. However, the assessment of their ability in harvesting energy from a dynamic oscillating source of mechanical energy is crucial to demonstrate their effectiveness in practical applications. This paper reports a first demonstration of a DEG system that is able to convert the oscillating energy carried by water waves into electricity. A DEG prototype is built using a commercial polyacrylate film (VHB 4905 by 3M) and an experimental campaign is conducted in a wave-flume facility, i.e. an artificial basin that makes it possible to generate programmed small-scale waves at different frequencies and amplitudes. In resonant conditions, the designed system demonstrates the delivery of a maximum of 0.87 W of electrical power output and 0.64 J energy generated per cycle, with corresponding densities per unit mass of dielectric elastomer of 197 W/kg and 145 J/kg. Additionally, a notable maximum fraction of 18% of the input wave energy is converted into electricity. The presented results provide a promising demonstration of the operation and effectiveness of ocean wave energy converters based on elastic capacitive generators.

1 Introduction

Renewable energy harvesting is a central topic of modern scientific and technological research. In the last decades, the effort to drive the consumption of primary energy resources towards an increasing share of “green energy” triggered scientific research on new technological solutions able to guarantee an efficient exploitation of renewable energy sources. In this context, several classes of devices based on innovative multifunctional materials have been investigated, in the attempt of providing disruptive new solutions for the direct mechanical-to-electrical energy conversion from environmental energy sources. Harvesting of energy from ambient vibrations and from air or liquid flows has been demonstrated through the use of piezoelectric [1, 2], electromagnetic [3, 4], triboelectric [5, 6] and electrostatic [7, 8] generators.

A particularly interesting class of such generators is represented by dielectric elastomer generators (DEGs) [9, 10]. DEGs are solid-state electrostatic converters made of one or more sheets of a compliant/highly-deformable dielectric material, coated with stretchable conductive electrodes. In terms of working principle, DEGs are variable capacitors, which allow the conversion of the mechanical work employed in their deformation into direct-current electricity. Since their first demonstration in the early 2000s [7], they have been studied in a number of applications such as energy harvesting from human motion, water currents, and sea waves [11, 12].

Compared to conventional electro-magnetic generators, DEGs undoubtedly enjoy simpler architectural solutions, lower mass density, reduced number of components, potentially higher reliability and lower cost. Such promising features attracted the interests of several researchers, that put their efforts into the enhancement of the performance of DEGs and the demonstration of their capability to effectively produce large power and electrical energy per unit dielectric elastomer (DE) material mass [13–15]. To date, energy densities of up to 1.15 kJ/kg have been demonstrated experimentally, using acrylic DEG samples subjected to equi-biaxial deformation [14]. In the last few years, these promising figures have awakened the interests of the ocean energy community, with specific reference to the emerging sector of wave energy. Ocean wave energy is an abundant and highly concentrated renewable energy source but its commercial exploitation is still limited to pilot installations and pre-commercial prototypes [16]. Current wave energy converters (WECs), based on conventional technologies, are showing excessive complexity and cost, poor resistance to the marine environment, and limited energy conversion efficiency. The introduction of DEGs can represent the technological breakthrough that provides the required boost to make wave energy exploitable [15, 17–20]. However, a systematic analytic evaluation and experimental demonstration of possible/effective solutions for converting the oscillating energy provided by waves into electricity using

DEGs has not been provided yet.

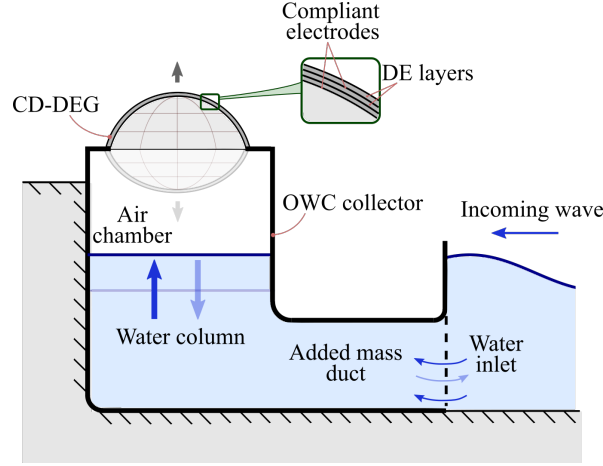


Figure 1: Schematic drawing of the DEG-OWC prototype, including a fixed-structure collector and a CD-DEG. Upward (downward) displacement of the water column free surface induces air compression (expansion) and upward (downward) CD-DEG deformation.

In this paper, we report on a first demonstration and experimental validation of a small-scale DEG-based WEC prototype, which has been conceived for a dynamic-resonant response tuned with prescribed wave frequencies. The prototype consists of a circular diaphragm DEG (CD-DEG) and a hydrodynamic interface (namely, a collector) that is shaped to canalize the oscillating water flux into a duct and to create a non-linear mass-spring oscillator. Due to the presence of this oscillating mass of water, the device, which is presented in Figure 1, takes the name of a DEG oscillating water column (DEG-OWC). The oscillating water column (OWC) architecture has been previously studied in the field of ocean energy in combination with more conventional types of power scavenging systems such as air turbines [21]. However, to date, the complexity and high costs of components, installation and maintenance of such converters, together with their reduced reliability and efficiency, have hindered their implementation in real commercial applications.

DEG-OWCs have been theoretically proposed and investigated in [22] showing their hypothetical implementation in large-scale wave energy applications. Additionally, experiments on a preliminary DEG-OWC small-scale prototype have been previously performed by some of the authors [23] in a wave-flume, i.e. a long and narrow tank for model testing in conditions of two-dimensional hydrodynamics and in the presence of artificially generated waves. These experiments demonstrated the generation of electrical power up to 67 mW with 1.9 grams of active DE material mass, which represents a limited amount compared to the power of the incident waves employed in those experiments. This limitation is mainly attributable to the

lack of an appropriate dynamical tuning of the prototype to the incoming waves.

In this work, we present the design and wave-flume testing of a new DEG-OWC prototype that is based on a dynamic-design rationale that takes into account the important contribution of the elastic response of the DE materials to the device dynamics. The system features a DEG sample made of a layer of polyacrylate DE (VHB 4905 by 3M) with a mass of 4.4 g, coated by a couple of carbon grease electrodes (MG-Chemicals 846). Thanks to this design approach, the device shows a highly tuned dynamic response that allows the conversion of power up to 0.87W, that represents a significant portion (up to 18%) of the wave energy impinging on the device.

The paper is organized as follows. Section 2 introduces the layout and working principle of the DEG-OWC system. Section 3 provides details on the dynamic model employed to design a resonant DEG-OWC. Section 4 describes the experimental setup and the working principle of the implemented controller. Section 5 illustrates the procedure for data processing/analysis and provides a discussion of the obtained results. Section 6 draws conclusions and illustrates future work.

The paper includes two Annexes that provide further information on the experimental procedures. Annex I describes the procedure used to estimate the deformation of the CD-DEG sample from acquired video frames. Annex II provides an experimental validation of an analytical expression used to estimate the CD-DEG sample capacitance.

2 Working principle

In this section, we describe the architecture of the small-scale DEG-OWC prototype under investigation. The system, represented in Figure 1, is composed of a circular diaphragm DEG (CD-DEG) and a rigid L-shaped collector that acts as a hydrodynamic interface. The CD-DEG is an inflatable polymeric unit generally made of one or more layers of DE material coated by compliant electrodes which are electrically connected to form a variable-geometry capacitor. The OWC-collector is a semi-submerged hollow structure, partially filled with water, having a water inlet at the bottom opened to the incoming wave field. An air volume (namely, the air chamber) is confined by the water surface (at the bottom), the walls of the collector (laterally) and the CD-DEG (at the top). In the equilibrium configuration, the CD-DEG is flat. As the waves impinge on the semi-submerged structure, the water column is put into reciprocating motion, which causes compressions-expansions of the entrapped air and the out-of-plane deformation (upward/downward inflation) of the CD-DEG.

The operation of the DEG-OWC is comparable to that of a non-linear oscillator, which

is excited by the sea waves and damped through the electrical control cycle of the CD-DEG, which enables the conversion of the incoming mechanical energy into electrical energy. In linear harmonic oscillators, the maximum energy transfer from the oscillating mechanical source to the damping load occurs when the natural frequency of the oscillating system matches the frequency of the excitation force [24]. For a wave energy converter, this means that the system should resonate under the effect of the incident wave. In the real world, sea waves are characterized by a superposition of several harmonics whose distribution presents significant time variability. Therefore, the device should feature a natural frequency that matches the typical (e.g., most probable or energetic) incoming wave frequency.

As shown in the following, the free dynamic response of the system is mainly governed by the inertia of the oscillating water mass and the stiffness associated with the hydrostatics, air chamber compressibility and the CD-DEG non-linear elasticity. In particular, the CD-DEG elasticity provides a significant contribution, leading to a global response of the system that is characterized by a highly non-linear behaviour. For such a complex dynamic system, the conditions at which the energy transfer is maximised cannot be trivially identified, but we assumed that a resonant-like behaviour should still be sought. In order to validate such an assumption, we consider an OWC architecture based on a collector which connects to the external sea environment through a horizontal duct, referred to as the added mass duct (see Figure 1). The purpose of the added mass duct is to canalize the water in order to increase the inertia of the oscillating water volume (resonating-mass).

In the following sections, a design rationale for the DEG-OWC is proposed through a definition of the resonance condition that takes into account the non-linear nature of the system. This makes it possible to tune the system so as to achieve resonance within a target frequency range. The design procedure makes use of a simplified but comprehensive model of the DEG-OWC dynamics. The design approach is validated through an experimental campaign conducted in a wave-flume basin at the University of Edinburgh.

3 Modelling and design

At a design stage, it is convenient to employ a simple model which captures only a minimum set of fundamental features. This model has to be appropriately calibrated in order to provide a sufficiently detailed description of the system response, while allowing fast computation and iteration on the design parameters. In this section, we describe a design-oriented numerical model for the DEG-OWC, which is composed of an electro-elastic sub-model for the CD-DEG and a hydrodynamic model for the OWC dynamics.

3.1 Dielectric elastomer generator model

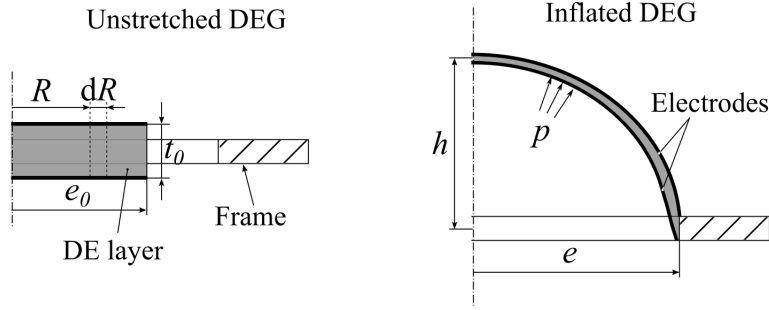


Figure 2: Schematic of the CD-DEG in the unstretched configuration (left) and in a generic inflated configuration (right).

The CD-DEG is modelled as an incompressible non-linear elastic non-viscous continuum, i.e. its volume is constant throughout deformation, and its mechanical response is governed by a hyper-elastic constitutive model [25]. Moreover, it is assumed that the elastomeric material within the CD-DEG behaves as an ideal dielectric, i.e., no current flows through the CD-DEG layers.

The geometry of the CD-DEG is depicted in Figure 2, where relevant dimensions are defined. The DEG radius and thickness in the flat unstretched configuration are e_0 and t_0 respectively (we neglect the electrodes thickness and assume that t_0 is entirely due to the DE material). Upon application of a radial pre-stretch λ_p , the radius becomes $e = \lambda_p e_0$.

The actual deformation under a uniform pressure difference, p , applied between the surfaces of the CD-DEG is generally described by complex deformation kinematics/dynamics, as pointed out in [26]. In order to develop a model with reduced complexity, we assume the simplifications proposed in [27]. Specifically, the deformation of the diaphragm is assumed as a perfectly spherical shell and the stretch is considered as equi-biaxial but with non-homogeneous value, i.e., stretch is variable with radius. Owing to these assumptions, the deformed geometry is uniquely identified by the diaphragm's tip elevation, h (positive for upward deformations), above the equilibrium plane, and the local stretch in this deformed configuration can be expressed as follows:

$$\lambda(h, R) = ee_0 \frac{h^2 + e^2}{e^2 e_0^2 + h^2 R^2}, \quad (1)$$

where R is the radius of the corresponding infinitesimal ring element in the undeformed configuration (see Figure 2).

We consider an infinitesimal variation of the CD-DEG state (i.e., deformation and electrical

state). The corresponding energy balance can be expressed in differential form as follows:

$$d\mathcal{W}_m + d\mathcal{W}_e = d\mathcal{E}_m + d\mathcal{E}_e \quad (2)$$

where the various differential terms have the following meaning and expressions:

- $d\mathcal{W}_m$ is the infinitesimal virtual work done by the pressure, p , in correspondence to a variation $d\Omega_c$ of the volume, Ω_c , which is bounded by the deformed spherical cap and the horizontal equilibrium plane:

$$d\mathcal{W}_m = p d\Omega_c. \quad (3)$$

The volume Ω_c (positive for upwards deformation) has the following equation:

$$\Omega_c(h) = \frac{\pi}{6} h(h^2 + 3e^2), \quad (4)$$

- $d\mathcal{W}_e$ is the infinitesimal work done by the conditioning circuit on the CD-DEG:

$$d\mathcal{W}_e = V dQ = CV dV + V^2 dC, \quad (5)$$

where V and Q are the CD-DEG voltage and charge respectively, and $C = Q/V$ is the capacitance in the present configuration, which has the following expression [27]:

$$C(h) = \frac{\pi \varepsilon e^2}{3t} \left[\left(\frac{h^2 + e^2}{e^2} \right)^3 + \left(\frac{h^2 + e^2}{e^2} \right)^2 + \left(\frac{h^2 + e^2}{e^2} \right) \right], \quad (6)$$

where ε is the dielectric constant of the DE material.

- $d\mathcal{E}_m$ is the infinitesimal variation of the elastic energy of the deformed elastomer, which reads as follows:

$$\mathcal{E}_m = \int_0^{e_0} 2\pi t_0 R \Psi(\lambda) dR, \quad (7)$$

where Ψ is the strain-energy function, that is, the local elastic volumetric energy density [25]. Assuming a constitutive relationship in Gent form [28], Ψ relates to the local equi-biaxial stretch as follows:

$$\Psi(\lambda) = -\frac{\mu J_m}{2} \log \left(1 - \frac{2\lambda^2 + \lambda^{-4} - 3}{J_m} \right), \quad (8)$$

where the shear modulus, μ , and Gent parameter, J_m , are constitutive constants.

- $d\mathcal{E}_e$ is the infinitesimal variation of the CD-DEG electrostatic energy, which reads as follows:

$$\mathcal{E}_e = \frac{1}{2} CV^2. \quad (9)$$

Upon rearrangement of Eqs. (2-9), the following equation for the equilibrium pressure difference, p , in a generic configuration is obtained:

$$p = \frac{d}{d\Omega_c} \int_0^{e_0} 2\pi t_0 R \Psi(\lambda) dR - \frac{V^2}{2} \frac{dC}{d\Omega_c}. \quad (10)$$

In the equation, λ (given by Eq. (1)) and C (Eq. (6)) are considered functions of Ω_c because they depend on h , which is in turn related to Ω_c by Eq. (4).

The net amount of electrical energy generated in correspondence to the infinitesimal deformation is given by:

$$d\mathcal{E}_e - d\mathcal{W}_e = -\frac{V^2}{2} dC, \quad (11)$$

and it shows that electrical energy is positively generated when the DEG capacitance decreases ($dC < 0$). On the contrary, if a voltage is applied on the CD-DEG while the capacitance is increasing, the device behaviour is reversed, electrostatic energy is absorbed by the device and converted into mechanical work.

The validity of the presented reduced model has been discussed in [27], showing that the mentioned assumptions (spherical deformed shape, equibiaxial stretch) provide a good agreement with FEM simulations in a wide range of DEG deformed configurations, such that $|h| \leq e$.

3.2 Hydrodynamic model

In this section, we describe the equation of motion of the OWC interface through the definition of lumped parameters. More specialistic models available in literature [21, 29, 30] are based on the employment of specific numerical codes and frequency-dependent hydrodynamic parameters, as well as the determination of wave diffraction from the device.

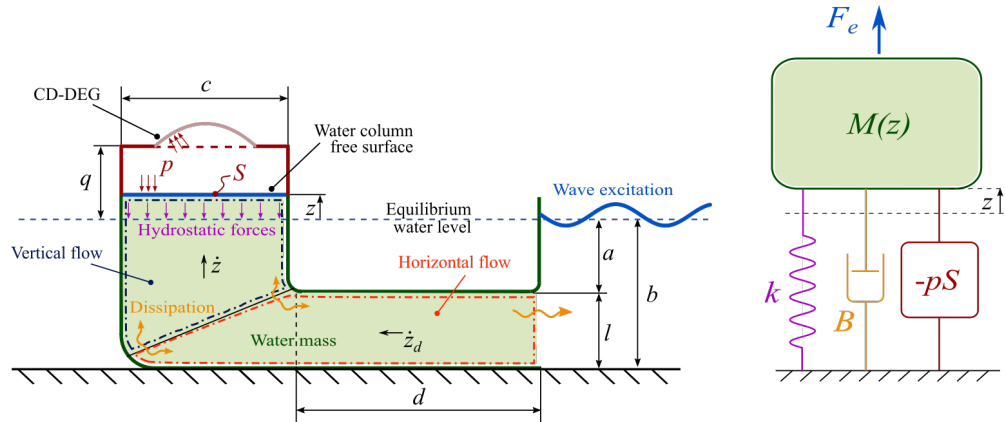


Figure 3: OWC collector dimensions and schematic of the lumped-parameter model.

Specifically, we choose a simplified two-dimensional dynamic model, based on simple analytic equations and on frequency-independent hydrodynamic parameters, as used in some other studies on OWCs [31]. Such an analytical approach allows the iterative update of the hydrodynamic parameters every time the design parameters (e.g., the collector dimensions) are changed, with no need for time-consuming software runs. Although this approach is rather simplified, it appears suitable at the design stage, as it allows the capturing of the essential features of the OWC's frequency response.

We consider a collector geometry with the dimensions identified in Figure 3. We assume that the water column free surface behaves as a rigid piston, i.e. it remains flat and horizontal during operation. A simplified velocity field of the water particles inside the collector is assumed. Specifically, we assume that the water volume enclosed by the collector can be ideally split into two parts, one featuring predominant horizontal flow (red dashed-dotted region in Figure 3), and the other featuring predominant vertical flow (blue dashed-dotted region in Figure 3). The region in between the added mass duct and the vertical water column has a mixed (horizontal/vertical) flow, therefore its contribution is equally split between the horizontal and vertical flow regions.

The displacement of the free surface from the equilibrium position is indicated by z ($z > 0$ for upward displacement). The water velocity within the added mass duct is denoted by \dot{z}_d and, due to mass conservation and water incompressibility

$$c\dot{z} = l\dot{z}_d, \quad (12)$$

where c and l are the collector dimensions reported in Figure 3. Under these assumptions the hydrodynamics of OWC is reduced to just one degree of freedom (the z variable is chosen) and the following general dynamic equation holds:

$$M(z)\ddot{z}(\tau) + B\dot{z}(\tau) + kz(\tau) = -p(\tau)S + F_e(\tau). \quad (13)$$

The symbols in Eq. (13) are defined in the following:

- τ is the time variable;
- \dot{z} and \ddot{z} are respectively the velocity and acceleration of the water column free surface;
- S is the area of the water column cross-section and is calculated as $S = cw$, where w is the width of the water channel.
- M is the inertia of the displacing water volume (reduced to coordinate z) and depends on z ; its expression can be derived from its kinetic energy formula, which includes the

contributions from both the horizontal and vertical flow regions respectively, and it can be consistently defined as follows:

$$M(z) = \rho S \left[\frac{(d + c/2)c}{l} + a + \frac{l}{2} + z \right]; \quad (14)$$

where a and d are geometric dimensions defined in Figure 3.

- B is the hydrodynamic damping coefficient, which takes into account hydraulic losses occurring within the OWC duct and the effect of radiated waves (generated by the water column oscillations); the determination of this coefficient is generally complex and requires a detailed simulation of the system hydrodynamics based, e.g., on computational fluid-dynamics techniques. The accurate calculation/prediction of B is beyond the scope of this work, however a sensitivity analysis is used to investigate the effect of B on the system resonance (see Section 3.3).
- k is the hydrostatic stiffness coefficient, which accounts for the restoring effect of gravity and it reads as $k = \rho g S$, where g is the gravitational acceleration.
- p is the gauge pressure in the closed air chamber (notice that the CD-DEG affects the OWC dynamics, and vice versa, through this contribution); and
- F_e is the time-dependent wave excitation force which depends on the wave-induced pressure on the collector inlet section. Neglecting diffraction from the device, the wave pressure equals the pressure of an undisturbed sinusoidal water wave (see Eq. (4.48) in [32]). A sinusoidal wave is fully described by its wave height, H , (crest to trough) and wave frequency, f . Integrating the pressure due to an undisturbed sinusoidal wave [32] over the collector inlet section, the wave excitation force on the OWC reads as follows:

$$F_e(\tau) = \rho g S \frac{H}{2} \frac{\sinh(k_w l)}{k_w l \cosh(k_w b)} \cos(2\pi f \tau), \quad (15)$$

where k_w is the wave number and can be calculated through the dispersion relation [32]:

$$g k_w \tanh(k_w b) = (2\pi f)^2. \quad (16)$$

It is worth noticing that the incident power carried by such a sinusoidal wave on a wave front with width w (as employed in the definition of efficiency used in Section 5) reads as follows:

$$P_w = \frac{\rho g^2 H^2 w}{32\pi f} \tanh(k_w b) \left[1 + \frac{2k_w b}{\sinh(2k_w b)} \right]. \quad (17)$$

Schematically, the OWC can be considered as a mass-spring-damper system with variable mass (see Figure 3 right), subjected to an excitation force F_e and to the non-linear action of the pressure force pS .

The coupling between the hydrodynamic and the CD-DEG models is obtained through the assumption of a uniform air pressure inside the close chamber, which is governed by isentropic transformations. When the membrane is flat, the air chamber volume is $V_0 = Sq$, and the absolute pressure in the chamber equals the atmospheric pressure, p_{atm} . Indicating with γ ($\gamma = 1.4$) the heat capacity ratio of air, the following equality holds:

$$p_{atm}V_0^\gamma = (p + p_{atm})(V_0 - Sz + \Omega_c)^\gamma. \quad (18)$$

3.3 Design

The objective of the design procedure for the DEG-OWC is to obtain a system able to convert a large fraction of the incoming wave energy into electricity. In order to achieve this goal, we design a DEG-OWC that, in the absence of electrical activation, has a natural frequency tuned to that of the incident waves.

It is well known that for a system whose response is described by linear dynamics, the maximum energy transfer occurs at resonance. This means that the natural frequency of the system is equal to the external excitation frequency, i.e. the wave-frequency. This condition is also known as “impedance matching” [24]. A linear dynamic one-degree-of-freedom system with inertia M and stiffness k has a natural frequency f_n given by the well-known relation $2\pi f_n = \sqrt{k/M}$. Such a natural frequency only depends on the dynamical system mechanical parameters (inertia and stiffness), regardless of the damping. The resonance condition occurs when the system is excited by a sinusoidal load with frequency equal to f_n . In resonance conditions, the power provided by the excitation force coincides with the power that is absorbed/dissipated by the damping loads in the system, while the mechanical powers associated with the time-varying kinetic energy and potential energy cancel each other out, i.e., their sum is identically equal to zero.

In the case of the DEG-OWC system, the resonance frequency cannot be defined through an elementary analytical condition due to its non-linear nature. Nonetheless, a consistent definition of resonance can be obtained using the above-mentioned energetic interpretation. With reference to the purely mechanical response (without electric activation) of dynamic system under investigation and to Eq. (13), we define the following mechanical power contributions:

- Power provided to the system by the excitation force: $P_e = F_e \dot{z}$.

- Active power associated with the hydrodynamic damping forces: $P_a = B\dot{z}^2$. This term is always positive and represents energy actively subtracted from the system.
- Reactive power associated with the oscillations of kinetic and potential energy (i.e., water gravitational energy, air internal energy, CD-DEG elastic energy): $P_r = (kz + pS + M\ddot{z})\dot{z}$. If the DEG is not electrically active and no dissipation occurs, this term has a null time average over an oscillation period.

Based on equation (13), the following identity can be immediately verified: $P_e(\tau) + P_a(\tau) + P_r(\tau) = 0$. At resonance (and in the absence of electrical activation), P_r is ideally null and the energy supplied to the system by the excitation force is entirely balanced by the dissipated active power. Owing to non-linearity, the existence of a steady state solution such that P_r is identically null is not guaranteed. Besides, the relative weight of P_r and P_a varies as the amplitude of the system excitation (e.g., the wave height) or the damping, B , vary. With reference to the CD-DEG operation in the absence of electrical activation, we considered the system resonant in a range of frequencies where the oscillations of P_r become small compared to the average active power.

The aim of the design procedure is that of providing a DEG-OWC with a resonance frequency within the operating frequency range of the experimental wave-flume facility (approximately, 0.6-1.2 Hz). The prototype is designed by iterating on the different geometric parameters and DEG features. For each combination of the design parameters, numerical simulations are run in order to solve Eq. (13) for a number of relevant wave parameters. In particular, a sensitivity analysis of the DEG-OWC dynamics to the excitation force amplitude and the hydrodynamic damping level (which is an otherwise uncertain parameter) is performed. Different sets of simulations are run, assuming that the DEG-OWC is impinged by sinusoidal waves with crest-to-trough height, H , and frequency, f [32]. In each set of simulations, the wave height, H , and the damping level, B , are kept constant, and the wave frequency, f , is varied throughout the different simulations. Different simulation sets, with different combinations of H and B values, are considered. The outcome of the design procedure are the DEG and OWC collector features presented in Table 1. The collector width, w , has been taken approximately equal to the tank width, to guarantee two-dimensional flow conditions.

The selected DE material for the CD-DEG is the commercial acrylic elastomer VHB 4905 produced by 3M. This material is widely employed as the DE in experiments [23, 33], as it is easy to pre-stretch and stack in layers. Additionally, VHB 4905 is particularly appropriate for the present small-scale resonant DEG-OWC application because it has low mechanical rigidity, thus putting a limit on the required amount of hydrodynamic inertia to achieve resonance.

Inlet sect. depth	$a = 0.15$ m	Material	VHB 4905 by 3M
Water depth	$b = 0.345$ m	Shear modulus	$\mu = 19.2$ kPa
Chamber breadth	$c = 0.37$ m	Gent parameter, J_m	$J_m = 427$
Duct length	$d = 0.60$ m	DEG stretched radius, e	125 mm
Duct height	$l = 0.20$ m	DEG unstretched thickness, t_0	1.5 mm
Air chamb. height	$q = 0.15$ m	Pre-stretch, λ_p	4
Device width	$w = 0.37$ m		

(a) Collector dimensions
(b) CD-DEG features

Table 1: Reference design features of the DEG-OWC collector and CD-DEG.

For this material, the constitutive parameters of the Gent hyperelastic model [28] to be used in Eq. 8 are also given in Table 1b, as found in [27].

A pre-stretch of $\lambda_p = 4$ has been selected. In general, the choice of an appropriate pre-stretch for DEGs featuring non-homogeneous deformation requires dedicated optimisations [34]. Here, the pre-stretch value has been chosen large enough to guarantee operation that is free from tension losses but limited in order to prevent excessive mechanical stiffness of the CD-DEG membrane. The reference CD-DEG features a DE volume of 4.6 cm^3 (i.e., approximately 4.4 g of mass). Based on the frequency range of the wave-flume facility (0.6-1.2 Hz) and on the expected convertible energy density (a few hundreds of J/kg, based on state-of-the-art experimental values [14, 15]), the expected power output of the device is around ~ 1 W. In practice, the maximum achievable power depends on the maximum DEG deformation achieved in dynamic operating conditions.

With reference to the selected design and material parameters, in Figure 4 we provide evidence of resonance achievement within the desired frequency range. The top subplot of the figure shows the ratio between the root mean square integral value of P_r (indicated by $P_{r,rms}$) and the mean integral value of P_a (indicated by $P_{a,avg}$) for steady-state periodic oscillations, as a function of the wave excitation frequency. Different curves refer to different simulation sets, as explained above.

In practice, the resonance frequency range can be defined as the interval where such a ratio has a minimum. By varying the external damping and the incident wave height, the natural frequency is predicted to remain within the range 0.6-0.8 Hz.

The bottom sub-plot shows the amplitude of the membrane tip oscillation $|h|$ (normalized by the diaphragm radius e) in the different scenarios, and it proves that the membrane deforma-

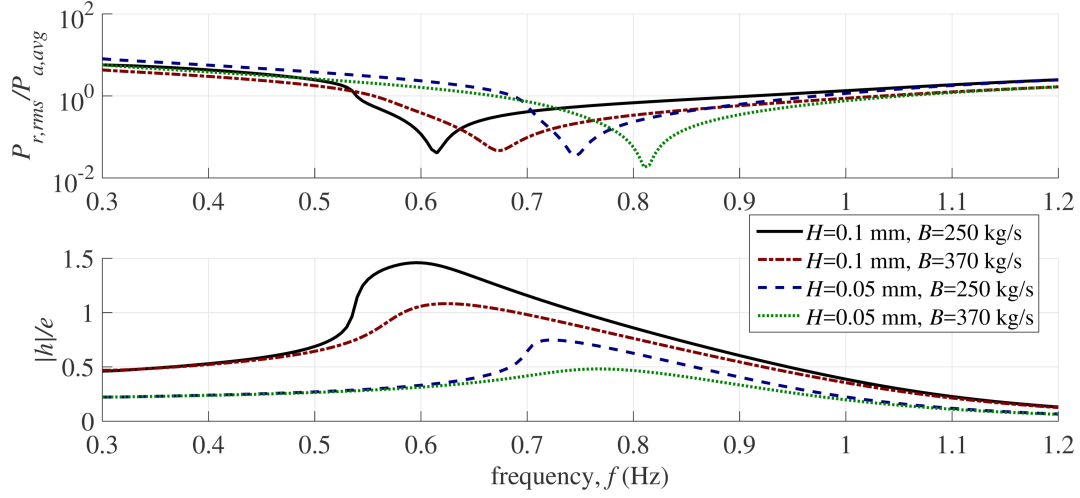


Figure 4: Response of the prototype in sinusoidal waves. The top plot is the ratio of the reactive power root mean square value to the mean active power (over a period), the bottom plot is the CD-DEG tip oscillation amplitude (divided by e).

tion is maximum approximately at the same frequencies that minimize $P_{r,rms}/P_{a,avg}$.

4 Experimental setup

A prototype has been designed based on the presented design specifications. The employed experimental prototype has been tested in the wave-flume facility available at the Hydraulics Laboratory at the School of Engineering, the University of Edinburgh [35]. The wave-flume is a twenty-meter-long channel with a width of 0.4 m, equipped, at one end, with a force-controlled absorbing paddle for wave generation. A wave absorbing beach, made of porous foam, is located at the other end of the tank. The mean water depth at the paddle is 0.7 m. The paddle can be controlled to produce sinusoidal waves with wave frequency, f , between 0.6 Hz and 1.2 Hz with maximum wave height, H , of 100 mm, although the maximum wave frequency can reach 1.6 Hz if the wave height is limited to 70 mm.

The DEG-OWC physical model (shown in Figure 5a) is made of different components, including the main mechanical and electronic subsystems described below.

4.1 Mechanical subsystem

The mechanical subsystem includes prototypes of the OWC collector and of the CD-DEG.

OWC collector. The DEG-OWC device is manufactured by assembling laser cut clear polycarbonate plates, which enables the visual inspection of the water column free surface

level within the OWC chamber. Different top panels for the added mass duct have been built, which allow the adjustment of the duct length. Nevertheless, in the described experiments, a length $d = 600$ mm has been chosen (as prescribed in Table 1a), as this has been observed to effectively provide resonating response within the expected frequency range. The top plate of the OWC structure has an aperture to which the CD-DEG is fastened using polycarbonate rings. The aperture has a radius $e = 0.125$ m. All the connections among the polycarbonate plates are sealed to prevent air/water leaks.

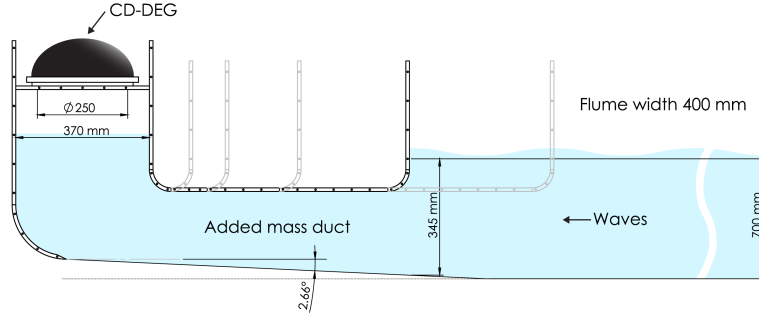
CD-DEG prototype. CD-DEG samples are manufactured using acrylic elastomer VHB 4905 as the DE material, and the electrodes are painted on using MG-Chemicals 846 conductive grease. As VHB 4905 layers are highly adhesive, the CD-DEG samples are made by bonding 3 DE layers on top of each other, each with a thickness of 0.5 mm (i.e., the unstretched membrane has a total thickness $t_0 = 1.5$ mm), and these are then pre-stretched to $\lambda_p = 4$. Connection of the compliant electrodes to the wires of the conditioning circuit is achieved using thin copper tape which is in contact, at one end, with the electrodes' perimeter, and are soldered, at the other end, to the circuit's wires.

A picture of the experimental prototype in operation is shown in Figure 5b. With respect to the proposed theoretical design, the prototype is positioned on an inclined sea-bed with a slope which reproduces shallow water conditions and sets the mean water depth at the device location to the desired level. The slope of the sea-bed is very limited (2.66°), thus the design assumptions outlined before (assuming a horizontal added mass duct) still hold.

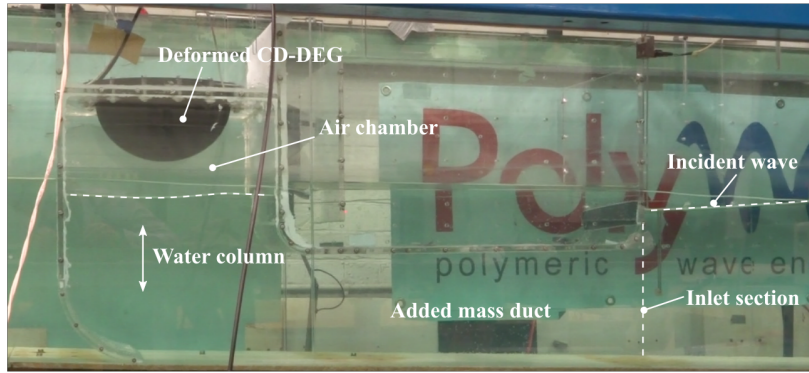
4.2 Electronics and sensing

A simple electronic circuit has been used to drive and control the CD-DEG, as shown in Figure 6a. The circuit includes: a high voltage (HV) power supply, a set of resistors (R_1 , R_2 and R_3), two HV switches, S_1 , S_2 , the CD-DEG (represented in the figure as a variable capacitor) and an in-parallel capacitor with constant capacitance $C_a = 78$ nF. A HV power supply 10C-125W by Ultravolt and reed relays HM12-1A69-150 by MEDER Electronics are employed. The use of the in-parallel capacitance (C_a) has been suggested in [14], as it limits the rise in voltage on the CD-DEG during operation, thus preventing the inception of electrical break-down, as explained in the following. Resistors R_1 and R_2 are used to limit currents during charging and discharging. Resistor R_3 is used to discharge the DEG at the end of each cycle, as also explained in the following.

All the HV connections are insulated with dielectric tape (the same VHB 4905) to avoid charge leaks in air. The energy harvesting controller of the DEG-OWC is implemented on a real-time machine (Performance real-time target machine by SpeedGoat) via the Matlab xPC



(a)



(b)

Figure 5: (a) Schematic drawing and (b) picture of the prototype during operation.

Target software environment. With regard to the measurements, a piezo-resistive pressure sensor (MPX12 by Freescale Semiconductor) is used to monitor the pressure within the air chamber. A custom-made high voltage probe, with 1000:1 dividing ratio and $10 \text{ G}\Omega$ resistance, is used to measure the voltage on the CD-DEG. The probe and pressure sensor signals are acquired at a sample frequency of 1 kHz, together with the commands for the opening and closing of the different relays, using the same real-time target machine used to control the CD-DEG. A high-speed camera (Point Grey GS3-U3-23S6M-C with lens 250F6C, using acquisition software FlyCapture 2.9) is used to film the CD-DEG deformation. Pictures are acquired at 100 fps. Time-series of the membrane tip elevation, h , are obtained by video frames post-processing using custom-made code based on computer graphic techniques (see details in Annex I). All the recorded signals (video frames, pressure, voltage, etc.) are synchronized with the same trigger activated from the target machine.

4.3 Control and generation cycles

The energy conversion cycle consists of the following operations:

- (1) *Capacitance increase.* The CD-DEG and C_a are connected to ground. The CD-DEG gets expanded upward or downward under the air pressure generated due to the raising or lowering of the water level in the chamber.
- (2) *Priming.* When its capacitance reaches the maximum value (generically denoted by C_{in}), switch S_1 is closed and the parallel CD-DEG and C_a are quickly charged up to a prescribed voltage V_{in} by the power supply. Switch S_1 is kept closed for a fixed time interval (very short compared to the generation cycle period, so that charging is nearly instantaneous).
- (3) *Generation.* The CD-DEG returns towards its flat configuration, S_1 is kept open and the total charge on the parallel capacitors is kept constant.
- (4) *Discharging.* The DEG is flat, its capacitance, C_{out} , is minimum, and the voltage, V_{out} , is maximum. The two capacitors are discharged through resistor R_3 , by closing switch S_2 . As in phase (2), S_2 is kept closed for a short amount of time, sufficient to guarantee complete discharging of the DEG and C_a .

It is worth noticing that during a wave period, the CD-DEG performs two energy generation cycles: one associated with the upward deformation and the other associated with the downward deformation of the DEG.

Triggering between successive phases of the generation cycle is based on real-time pressure measurements in the air chamber. In particular, triggering between states (1) and (2) is enabled using the time derivative of the pressure signal; triggering between states (3) and (4) is obtained by monitoring the inversion of the relative pressure sign.

In terms of electrical variables (charge, Q , and voltage, V), the control cycle described above is graphically represented in Figure 6b (black solid line). Priming phase (2) of the generation cycle coincides with transformation OA in the picture; generation phase (3) is AB, discharging (4) is BO. The capacitance increase phase (1), which is a purely mechanical transformation, is not visible in the plot.

The charging and discharging phases are represented by two straight iso-capacitance lines (OA and BO respectively), corresponding to two distinct values of the DEG capacitance: C_{in} and C_{out} respectively. In particular, the DEG capacitance during the charging phase, C_{in} , depends on the maximum deformation reached by the DEG at each cycle. Besides varying throughout the different cycles, C_{in} may undergo some variations during the charging phase of a given

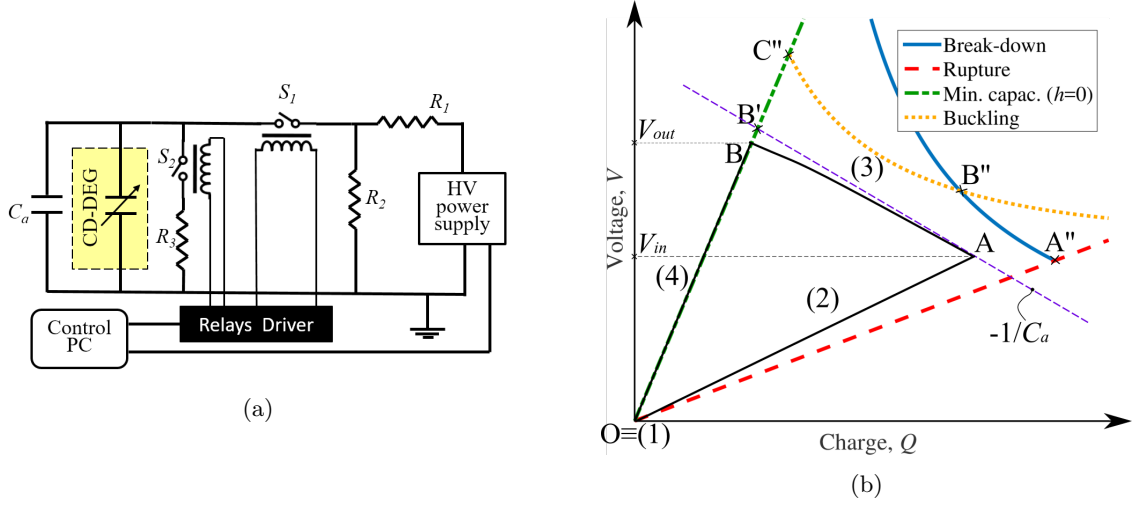


Figure 6: (a) Electronic circuit to drive the CD-DEG. (b) Charge-voltage ($Q - V$) diagram providing a qualitative representation of the CD-DEG operating constraints and an example of theoretical and real energy generation cycles.

cycle, due to variations in the DEG shape induced by the electrical stresses owing to the fast rise of the electric field across the DE layer. However, in the case under investigation, this effect is negligible and the DEG capacitance can be considered constant throughout the charging process. Capacitance C_{out} is constant throughout the different cycles, as instantaneous DEG discharging takes places while the CD-DEG is in equilibrium in the flat configuration.

Curve AB theoretically coincides with a straight line with slope $-C_a^{-1}$ (line AB'). Owing to charge conservation, indeed, voltage, V , and charge Q on the CD-DEG during phase (3) are related by the following equation:

$$Q = Q_t - C_a V, \quad (19)$$

where Q_t is the total charge on the CD-DEG and the in-parallel capacitor C_a during phase (3), and it depends on the prescribed priming voltage, V_{in} , and on the maximum capacitance reached by the DEG in the considered cycle. In practice, owing to charge leakage through the DE layers, curve AB slightly differs from theoretical line AB' (see Figure 6b), as the final charge (in state B) is lower than in ideal conditions (state B').

Notice that, for a proper choice of C_a , when the DEG reaches a large deformation, cycle OABO should well approximate cycle OA''B''C''O, which is a qualitative representation of the theoretical maximum-energy conversion cycle, and depends on the physical limitations of the material (namely, mechanical rupture, electrical break-down, buckling/instability). The representation of the limit curves on the $Q - V$ diagram can be accomplished based on the DE

material properties (break-down electric field, rupture stretch, etc.) and on the constitutive equations for the considered DEG topology [13, 22].

It is worth noticing that the proposed conditioning circuit (shown in Figure 6a) is used in the presented experiments for the purpose of demonstration, as it allows straightforward implementation of the control cycle described above and estimation of the generated electrical power (see Section 5.1). However it does not provide storage capability of the generated electrical energy. Scalable electronic solutions for the driving of DEGs require more sophisticated topologies, as proposed in [36].

5 Data post-processing and results

Tests have been performed using a wide set of wave parameters (frequency and wave height) and at priming voltages, V_{in} , within limits that are safely chosen to keep the electric field below 80% of the breakdown electric field of the dielectric. Specifically, the following parameters have been employed: wave frequency f , from 0.5 Hz to 1.1 Hz, in steps of 0.2 Hz; crest-to-trough wave heights, H , of 30, 60 and 90 mm; priming voltage of 3500, 4000 and 4300 V. In each test, the wave-flume has been started from a fully-flat condition. For each test, 5 to 8 wave periods with the CD-DEG inactive and 5 to 8 wave periods with the CD-DEG active have been recorded. A total of 36 test-runs have been performed and acquired, collecting approximately 700 s of time-series.

5.1 Data post-processing

With the aim of characterizing the device converted power and wave capture efficiency, the following variables have been measured: 1) voltage, V , on the CD-DEG and the in-parallel capacitance C_a , 2) membrane tip displacement, h , from the horizontal DEG equilibrium plane ($h > 0$ for upward deformation), obtained from the video frames of a high-speed camera (as described in Annex I).

From the membrane tip displacement time-series, it is possible to compute the evolution in time of the capacitance C of the CD-DEG, which relates to h as per Eq. (6) ($\epsilon = 4.2 \cdot 8.81 \cdot 10^{-12}$ F/m for VHB 4905). The validity of Eq. (6) has been verified (in the range of interest, i.e., approximately $|h| \leq e$) via static measurements performed on the CD-DEG sample, as described in Annex II.

Figure 7 provides a schematic representation of the electrical energy fluxes through the CD-DEG and capacitance C_a in a cycle. In the figure, Q and V stand for the CD-DEG charge and voltage, while Q_a and V_a are the same variables measured on capacitance C_a .

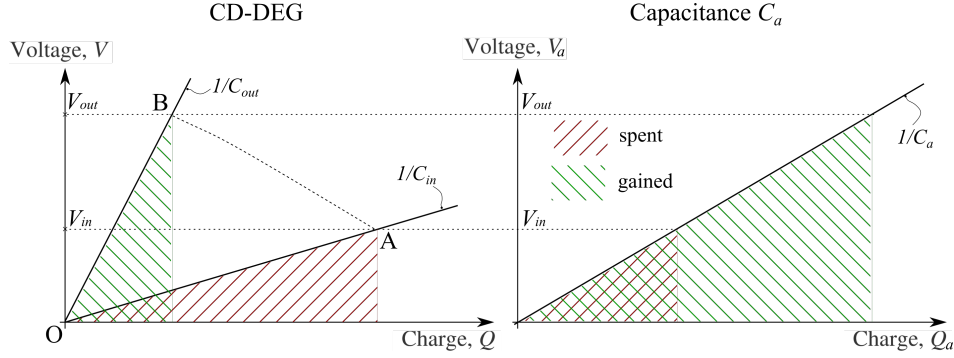


Figure 7: Schematic representation (on charge-voltage diagrams) of the energy fluxes through the CD-DEG and in-parallel capacitance C_a during a generation cycle.

With reference to the notation in Figure 6b, the two capacitors exchange electrical energy with the conditioning circuit only during phases (2) and (4). Indeed, during phase (3), the system of the two capacitors is isolated, and the DEG transfers energy on C_a as its capacitance decreases. Phase (1) is, on the contrary, a purely mechanical transformation.

During phase (2), an amount of electrical energy is spent to charge the DEG and the in-parallel capacitor (numerically equal to the red hatching in Figure 7). During phase (4), an amount of energy is gained by fully discharging the two capacitors (green hatching in Figure 7).

The net electrical energy generated in the i -th cycle is indicated by $E_{g,i}$ and is given by:

$$E_{g,i} = \frac{1}{2}C_{out}V_{out,i}^2 - \frac{1}{2}C_{in,i}V_{in,i}^2 + \frac{1}{2}C_a(V_{out,i}^2 - V_{in,i}^2), \quad (20)$$

where $V_{in,i}$ and $V_{out,i}$ are respectively the voltages on the CD-DEG (and on C_a) respectively at the end of the charging and discharging phases of the i -th cycle, while $C_{in,i}$ and C_{out} represent the CD-DEG capacitance during the charging and discharging phases (with C_{out} being constant throughout the different cycles as it represents the capacitance of the flat CD-DEG). The first two terms in the equation account for the positive (gained) and negative (spent) energy fluxes through the DEG respectively, while the third term accounts for the global balance on the in-parallel capacitor.

Equation (20) only requires knowledge of voltage and DEG capacitance estimates at points A and B of the generation cycle (see Figure 6b). Notice that the amount of energy generated during phase (2) is calculated from the energy balance on C_a , and does not require knowledge of the exact shape of curve AB (see Figure 6b).

The average power is calculated from $E_{g,i}$ values as follows:

$$P_g = \frac{1}{t_{tot}} \sum_{i=1}^N E_{g,i}, \quad (21)$$

where N is the total number of generation cycles in a test-run, which take place over a time span $t_{tot} = N/(2f)$ (note that two generation cycles are performed for each wave period).

The average energy density (per unit DE material mass) harvested in a cycle (i.e., half a wave period) can be then defined as follows:

$$e_g = \frac{P_g}{2\pi\rho_p t_0 e_0^2 f} = \frac{1}{N\pi\rho_p t_0 e_0^2} \sum_{i=1}^N E_{g,i}. \quad (22)$$

where $\rho_p = 960 \text{ kg/m}^3$ is the volumetric mass density of VHB 4905 [7].

A further figure of merit for the device is the so-called wave-to-wire efficiency, that is the fraction of the incoming wave power effectively converted into electrical energy, namely:

$$\beta = \frac{P_g}{P_w}. \quad (23)$$

The power P_w of a sinusoidal sea wave with frequency f and height H is given by Eq. (17).

5.2 Experimental results

In this section, we report experimental results, i.e., relevant time-series and figures of merit defined above, over the different experimental test sets. Figure 8 shows examples of time-series of air relative pressure, p , CD-DEG tip displacement, h , and voltage V on the CD-DEG. Three different test runs are presented, which feature the same priming voltage ($V_{in} = 4000 \text{ V}$) and incident wave height ($H = 60 \text{ mm}$), and different wave frequencies f . In the three cases, the time-series show a first phase during which no electrical activation is present on the membrane, and a second phase during which the CD-DEG is electrically driven according to the control cycle described in Section 4.3.

The plots show that the oscillation amplitude of the CD-DEG is maximum at $f = 0.7 \text{ Hz}$, i.e., at that frequency the system shows a close-to-resonance behaviour.

The oscillation amplitudes of p and h in the first half of the time intervals (when no electric activation is present) and in the second half of the time intervals (when the CD-DEG is actively controlled) are different. In particular, the oscillation amplitude in the presence of activation decreases for $f = 0.7$ and 0.9 Hz , while it remains approximately constant (or slightly increases) for $f = 0.5 \text{ Hz}$. Electric activation has indeed two effects on the dynamics: 1) it damps the system oscillation, as it subtracts energy from the system oscillations in the form of electrical energy; 2) it makes the DEG rigidity decrease, because the electrical stress induces a relaxation of the total stress of the material [10], thus slightly shifting the natural frequency of the system towards lower frequencies. The system natural frequency (in the absence of charge) is about 0.7 Hz . When the DEG is activated, the oscillation amplitudes

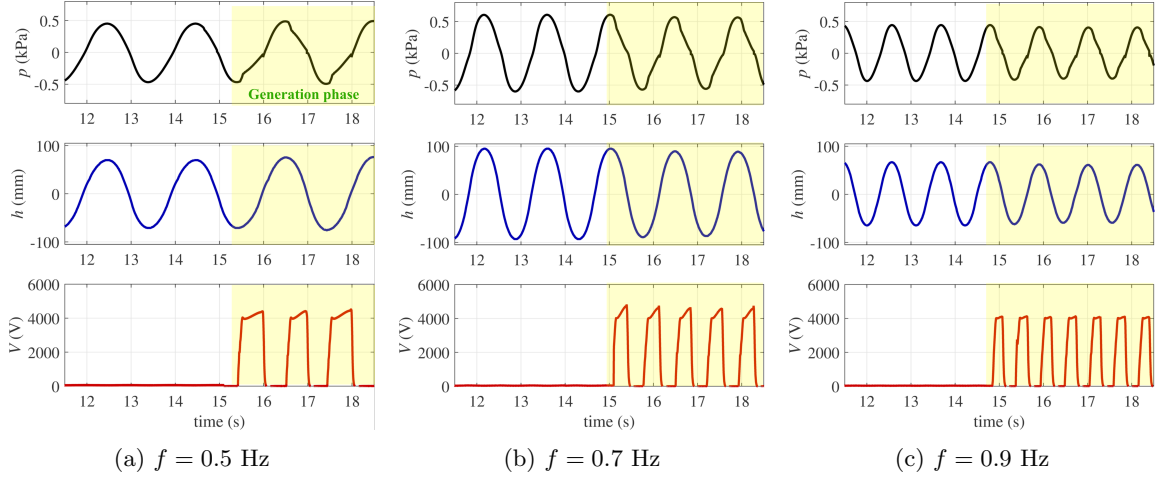


Figure 8: Time-series of gauge pressure, p , tip height, h and CD-DEG voltage V for three tests featuring $H = 60$ mm, $V_{in} = 4000$ V and different wave frequency f . Highlighted areas refer to phases during which the DEG is actively controlled.

at wave frequencies $f \geq 0.7$ Hz decrease, both because the system is damped and because the natural frequency becomes lower than the excitation frequency. At 0.5 Hz, when electric activation is provided, the excitation frequency gets closer to the natural frequency, thus compensating the increase in damping.

With reference to three different values of the priming voltage, V_{in} , experimental figures of merit (P_g , e_g , β) for the DEG-OWC prototype operation are shown in Figure 9a. Each marker in the plots refers to an individual test run with specified wave height and frequency. In general, the plots show that the converted energy is maximum at a frequency of 0.7 Hz (i.e., the frequency at which the DEG-OWC system resonates) and is rather independent of the level of electrical loading and the amplitude of the incident wave. The device performs significantly better when it resonates with the incoming waves, thus highlighting that dynamic tuning is crucial for the operation of DE-based WECs.

At a prescribed frequency, power output and converted energy density increase with increasing wave height H , as a result of the increased incident wave power. Although the incident wave power increases quadratically with H (see Eq. (17)), the device power output increases less than quadratically (especially at larger wave heights), most probably due to the saturation in the DEG deformation and to larger electro-mechanical losses in the presence of larger displacements/velocities.

The wave-to-wire conversion efficiency is minimum at the smallest wave height ($H = 30$ mm). In effect, when the CD-DEG undergoes small deformations, its capacitance variation is very

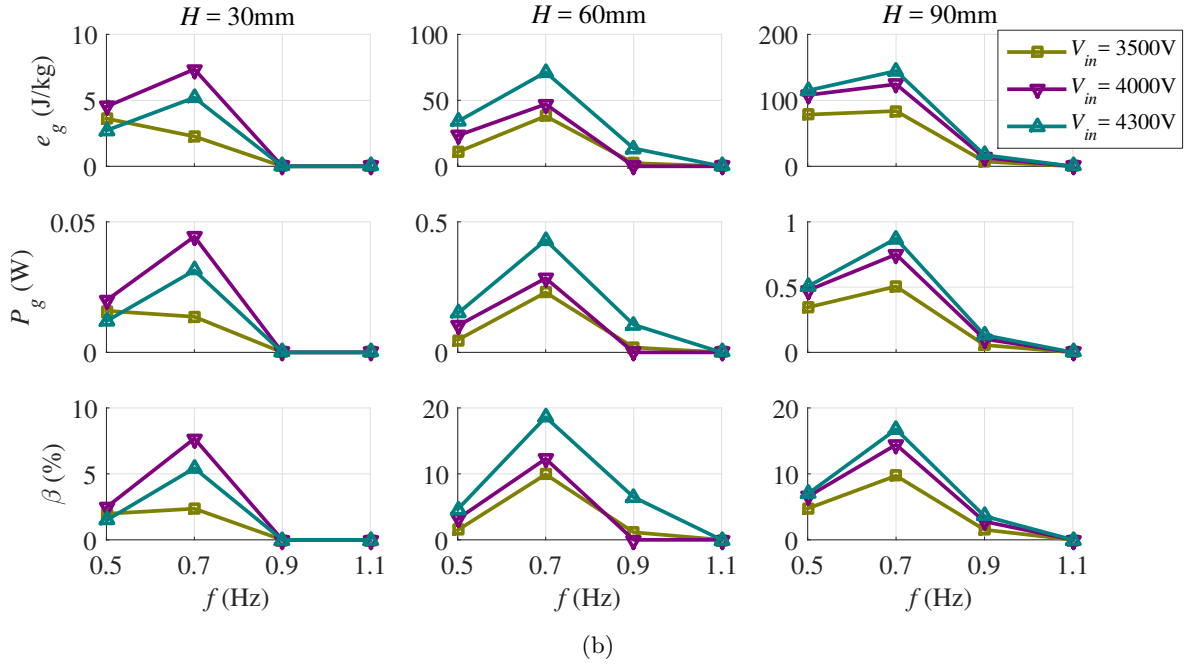
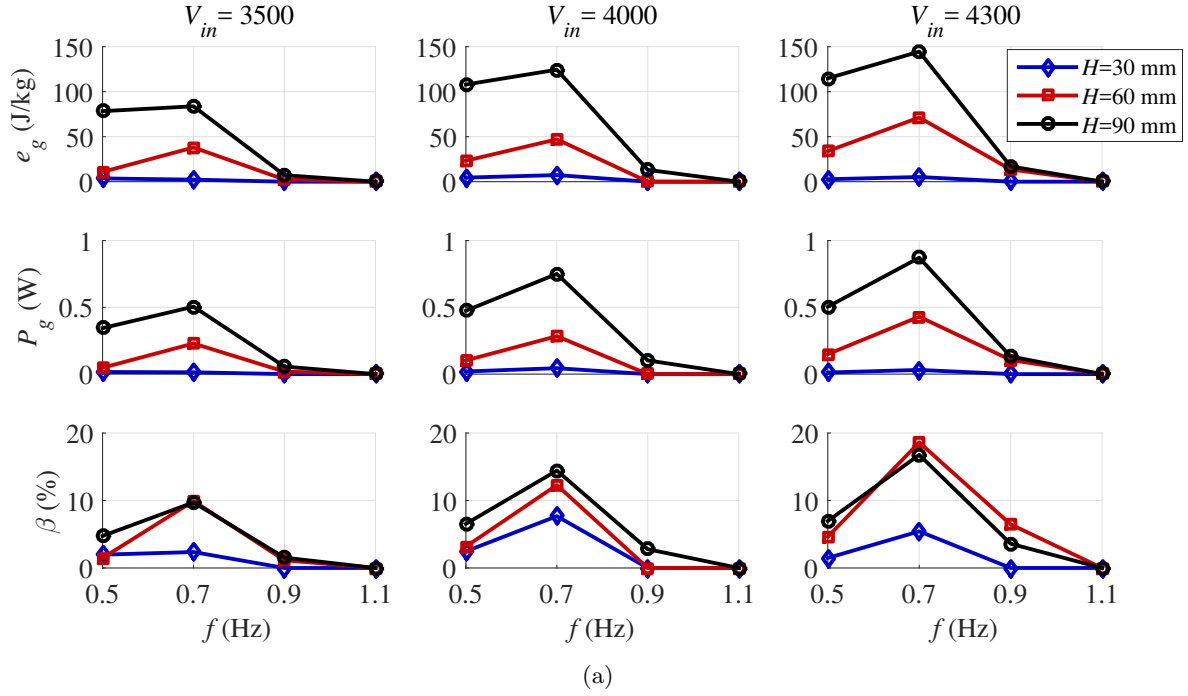


Figure 9: Experimental figures of merit (e_g , P_g , β) for the DEG-OWC prototype as a function of the excitation frequency. (a) Data are sorted by priming voltage, V_{in} , with line colours corresponding to different wave heights, H . (b) Data are sorted by wave height, H , with line colours corresponding to different priming voltages, V_{in} .

limited (Eq. (6) shows that the derivative of C at $h = 0$ is null), while capacitance variation dramatically increases with increasing h . The efficiencies at wave heights H of 60 and 90 mm are approximately equal. Possible explanations for this behaviour are that the CD-DEG deformation tends to saturate with increasing wave heights, and the increase in capacitance variation at larger deformations (at $H = 90$ mm) is counterbalanced by the higher electro-mechanical dissipations.

Figure 9b shows the different figures of merit as a function of the incident wave frequency and priming voltage, for three different sets of data relative to different wave heights. The plots show that the increase of voltage generally leads to an improvement in the device performance, except for the case with $H = 30$ mm, where performance with $V_{in} = 4000$ V is better than with $V_{in} = 4300$ V. In effect, in the presence of weak incident waves, a high level of electrical loading might provide the system with an excessive damping, thus negatively affecting the performance. It is expected that, even at larger wave heights, optimal levels of electrical loading exist which compromise between excessively low voltages (which provide low convertible energy density) and excessive voltages, which would damp the system too much. However, in large waves, such optimal values of priming voltage may be larger than the admissible values set by the material failure modes [13].

The maximum generated energy density reaches approximately 145 J/kg, which is a relevant value for a practical field application. This figure is slightly lower with respect to maximum results obtained with the same DE material in prior state of the art experiments with prescribed deformation [14]. However, it should be highlighted that the experimental conditions for the present work shows several differences with respect to previous experiments, including: (1) the type of energy source: the energy is converted from a dynamic source of energy and not from a source that imposes controlled deformations; (2) the number of repeated generation cycles: in the present experiments results are obtained as averages over a number cycles; (3) the level of stress: electrical and mechanical stresses are purposely kept below prescribed threshold in order to guaranty durability and repeatability; (4) the type of deformation: CD-DEGs have a rather simple architecture but undergo non-uniform deformations, so the employed DE material cannot be exploited to its maximum capability.

In these conditions the maximum produced power is about 870 mW. From this value, the power capability of a full-scale device able to convert the energy of (real-scale) ocean waves can be estimated by applying rules for WEC prototypes scaling based on Froude scaling [37]. Small-scale waves at which the system is resonating have a frequency of approximately 0.7 Hz, while real waves with relevant energy content are in the range of 0.1-0.12 Hz [32]. According to Froude scaling rules, wave frequency is downscaled with the square root of the scaling

factor. Thus, the scale factor can be found in the range of 30-50. Based on Froude scaling, the real-scale power can be estimated as the power of the small scale device times the scale factor elevated to the power of 3.5. This means that the maximum power of the equivalent real-scale device lies in the range of hundreds of kilowatts (130-770 kW).

This is a very encouraging figure, which provides an important proof for the viability of DEG technology for the ocean wave energy sector. Additionally, such figures have large room for improvements since the employed DE material exhibits large visco-elasticity and charge leakages, which affect the CD-DEG efficiency [26]. A significant improvement in the device performance may be achieved on larger-scale systems, where the acrylic elastomer could be replaced with better performing materials such as natural or synthetic rubbers [15, 38, 39]. The comparison between DEGs made of rubber and of VHB acrylic has been addressed in [34] theoretically and in [15] with experiments, demonstrating rubber capability to convert larger energy densities. Such alternative DE materials are not suitable for small scale tests due to their large elastic stiffness, which prevents the practical implementation of the resonant design presented in this article, while at large scale the use of stiffer materials, featuring an elastic modulus increased by the scale factor, would result in an equivalent dynamical response according to Froude scaling. Improvements are also possible through improvement of the OWC collector design, aimed at reducing sloshing within the water column chamber and hydrodynamic losses in general. Finally, the full-scale deployment of DEG-based WECs requires the design and implementation of scalable power electronics, capable of implementing efficient DEG charging and discharging.

6 Conclusions

We have presented and demonstrated a DEG-OWC, an innovative architecture of a sea wave energy converter (WEC) based on a dielectric elastomer generator (DEG) that makes it possible to convert wave energy into electricity. The proposed system is based on an inflatable circular diaphragm DEG (CD-DEG), i.e. an electrostatic variable capacitor, made of an acrylic dielectric layer (VHB 4905) and compliant electrodes. The CD-DEG is coupled to a non-linear harmonic oscillator composed of a collector that confines a mass of water, i.e. an oscillating water column (OWC), which is put into reciprocating motion by the hydrodynamic pressure of water waves. Upon adequate electrical control, the CD-DEG is able to implement the conversion of a relevant fraction of the incoming wave power into direct-current electricity. We proposed a design approach aimed at providing resonant response of the system, which maximizes the converted power within a prescribed range of wave frequencies.

A small-scale prototype of DEG-OWC has been designed and tested in a wave-flume basin in different sinusoidal wave conditions and with different levels of electrical loading. Experimental results show a maximum electrical power output of up to 0.87 W and demonstrate that a relevant fraction (up to 18%) of the wave power can be converted into electricity. Maximum energy density per cycle and per unit dielectric material mass of 145 J/kg has been obtained which proves that, even in combination with a dynamical source of mechanical power, DEGs can achieve large values for this figure of merit.

These results are likely to have a relevant impact on future practical applications in the field of ocean energy. Indeed, according to the scaling rules criteria for wave energy systems, the power output measured on the small-scale prototype corresponds to hundreds of kilowatt for the equivalent full-scale system [37].

In future works, further ameliorations could be attained by the employment of improved materials for both the dielectric layers and the compliant electrodes, with reduced electro-mechanical losses and scalable manufacturing to enable the development and deployment of larger scale devices.

Acknowledgements

The research leading to these results has received funding from the European Union Seventh Framework Programme [FP7/2007-2013] under grant agreement n° 309139.

The authors would like to thank Mr. Jean-Baptiste Richon (The University of Edinburgh) and Mr. Francesco Damiani (Scuola Superiore Sant’Anna) for their invaluable help during the experimental tests, and Mr. Sandro Okutuga (former student at Scuola Sant’Anna) for his support during data post-processing.

References

- [1] K. Cook-Chennault, N. Thambi, and A. Sastry, “Powering mems portable devicesa review of non-regenerative and regenerative power supply systems with special emphasis on piezoelectric energy harvesting systems,” *Smart Materials and Structures*, vol. 17, no. 4, p. 043001, 2008.
- [2] A. Erturk, W. Vieira, C. De Marqui Jr, and D. Inman, “On the energy harvesting potential of piezoaeroelastic systems,” *Applied Physics Letters*, vol. 96, no. 18, p. 184103, 2010.

- [3] S. P. Beeby, R. Torah, M. Tudor, P. Glynn-Jones, T. O'donnell, C. Saha, and S. Roy, "A micro electromagnetic generator for vibration energy harvesting," *Journal of Micromechanics and microengineering*, vol. 17, no. 7, p. 1257, 2007.
- [4] B. Yang, C. Lee, W. Xiang, J. Xie, J. H. He, R. K. Kotlanka, S. P. Low, and H. Feng, "Electromagnetic energy harvesting from vibrations of multiple frequencies," *Journal of Micromechanics and Microengineering*, vol. 19, no. 3, p. 035001, 2009.
- [5] X. Wang, S. Niu, Y. Yin, F. Yi, Z. You, and Z. L. Wang, "Triboelectric nanogenerator based on fully enclosed rolling spherical structure for harvesting low-frequency water wave energy," *Advanced Energy Materials*, vol. 5, no. 24, 2015.
- [6] Z. Quan, C. B. Han, T. Jiang, and Z. L. Wang, "Robust thin films-based triboelectric nanogenerator arrays for harvesting bidirectional wind energy," *Advanced Energy Materials*, vol. 6, no. 5, 2016.
- [7] R. Pelrine, R. D. Kornbluh, J. Eckerle, P. Jeuck, S. Oh, Q. Pei, and S. Stanford, "Dielectric elastomers: generator mode fundamentals and applications," in *SPIE's 8th Annual International Symposium on Smart Structures and Materials*, pp. 148–156, International Society for Optics and Photonics, 2001.
- [8] D. Peter, R. Pichler, S. Bauer, and R. Schwödiauer, "Electrostatic converter with an electret-like elastomer membrane for large scale energy harvesting of low density energy sources," *Extreme Mechanics Letters*, vol. 4, pp. 38–44, 2015.
- [9] F. Carpi, D. De Rossi, R. Kornbluh, R. E. Pelrine, and P. Sommer-Larsen, *Dielectric elastomers as electromechanical transducers: Fundamentals, materials, devices, models and applications of an emerging electroactive polymer technology*. Elsevier, 2011.
- [10] Z. Suo, "Theory of dielectric elastomers," *Acta Mechanica Solida Sinica*, vol. 23, no. 6, pp. 549–578, 2010.
- [11] R. D. Kornbluh, R. Pelrine, H. Prahlaad, A. Wong-Foy, B. McCoy, S. Kim, J. Eckerle, and T. Low, "From boots to buoys: promises and challenges of dielectric elastomer energy harvesting," in *Electroactivity in Polymeric Materials*, pp. 67–93, Springer, 2012.
- [12] R. D. Kornbluh, J. Eckerle, and B. McCoy, "A scalable solution to harvest kinetic energy," *SPIE Newsroom*, 2011.

- [13] S. J. A. Koh, C. Keplinger, T. Li, S. Bauer, and Z. Suo, “Dielectric elastomer generators: how much energy can be converted?,” *IEEE/ASME Transactions on mechatronics*, vol. 16, no. 1, pp. 33–41, 2011.
- [14] S. Shian, J. Huang, S. Zhu, and D. R. Clarke, “Optimizing the electrical energy conversion cycle of dielectric elastomer generators,” *Advanced Materials*, vol. 26, no. 38, pp. 6617–6621, 2014.
- [15] R. Kaltseis, C. Keplinger, S. J. A. Koh, R. Baumgartner, Y. F. Goh, W. H. Ng, A. Kogler, A. Tröls, C. C. Foo, Z. Suo, and S. Bauer, “Natural rubber for sustainable high-power electrical energy generation,” *RSC Advances*, vol. 4, no. 53, pp. 27905–27913, 2014.
- [16] A. Falcão, “Wave energy utilization: A review of the technologies,” *Renewable and sustainable energy reviews*, vol. 14, no. 3, pp. 899–918, 2010.
- [17] P. Jean, A. Wattez, G. Ardoise, C. Melis, R. Van Kessel, A. Fourmon, E. Barrabino, J. Heemskerk, and J. Queau, “Standing wave tube electro active polymer wave energy converter,” in *SPIE Smart Structures and Materials+ Nondestructive Evaluation and Health Monitoring*, International Society for Optics and Photonics, 2012.
- [18] S. Chiba, M. Waki, T. Wada, Y. Hirakawa, K. Masuda, and T. Ikoma, “Consistent ocean wave energy harvesting using electroactive polymer (dielectric elastomer) artificial muscle generators,” *Applied Energy*, vol. 104, pp. 497–502, 2013.
- [19] B. Scherber, M. Grauer, and A. Köllnberger, “Electroactive polymers for gaining sea power,” in *SPIE Smart Structures and Materials+ Nondestructive Evaluation and Health Monitoring*, International Society for Optics and Photonics, 2013.
- [20] G. Moretti, M. Fontana, and R. Vertechy, “Model-based design and optimization of a dielectric elastomer power take-off for oscillating wave surge energy converters,” *Meccanica*, vol. 50, no. 11, pp. 2797–2813, 2015.
- [21] A. F. Falcão and J. C. Henriques, “Oscillating-water-column wave energy converters and air turbines: A review,” *Renewable Energy*, vol. 85, pp. 1391–1424, 2016.
- [22] G. Moretti, G. P. Rosati Papini, M. Alves, M. Grases, R. Vertechy, and M. Fontana, “Analysis And Design of an Oscillating Water Column Wave Energy Converter with Dielectric Elastomer Power Take-Off,” in *ASME 2015 34th International Conference on Ocean, Offshore and Arctic Engineering*, American Society of Mechanical Engineers, 2015.

- [23] R. Vertechy, M. Fontana, G. Rosati Papini, and D. Forehand, “In-tank tests of a dielectric elastomer generator for wave energy harvesting,” in *SPIE Smart Structures and Materials+ Nondestructive Evaluation and Health Monitoring*, International Society for Optics and Photonics, 2014.
- [24] J. Falnes, *Ocean waves and oscillating systems: linear interactions including wave-energy extraction*. Cambridge University Press, 2002.
- [25] G. A. Holzapfel, *Nonlinear solid mechanics - A continuum approach for Engineering*, vol. 24. Wiley Chichester, 2000.
- [26] T. Li, S. Qu, and W. Yang, “Energy harvesting of dielectric elastomer generators concerning inhomogeneous fields and viscoelastic deformation,” *Journal of Applied Physics*, vol. 112, no. 3, p. 034119, 2012.
- [27] R. Vertechy, G. P. P. Rosati, and M. Fontana, “Reduced model and application of inflating circular diaphragm dielectric elastomer generators for wave energy harvesting,” *Journal of Vibration and Acoustics*, vol. 137, no. 1, pp. 011016–1–011016–9, 2015.
- [28] A. Gent, “A new constitutive relation for rubber,” *Rubber chemistry and technology*, vol. 69, no. 1, pp. 59–61, 1996.
- [29] J. Newman and C.-H. Lee, “Boundary-element methods in offshore structure analysis,” *Journal of Offshore Mechanics and Arctic Engineering*, vol. 124, no. 2, pp. 81–89, 2002.
- [30] G. Malara, R. Gomes, F. Arena, J. Henriques, L. Gato, and A. Falcão, “The influence of three-dimensional effects on the performance of u-type oscillating water column wave energy harvesters,” *Renewable Energy*, 2017.
- [31] P. Boccotti, “Caisson breakwaters embodying an owc with a small opening - part i: Theory,” *Ocean Engineering*, vol. 34, no. 5, pp. 806–819, 2007.
- [32] M. E. McCormick, *Ocean wave energy conversion*. Dover Publications, Inc, 2007.
- [33] R. Kaltseis, C. Keplinger, R. Baumgartner, M. Kaltenbrunner, T. Li, P. Mächler, R. Schwödiauer, Z. Suo, and S. Bauer, “Method for measuring energy generation and efficiency of dielectric elastomer generators,” *Applied Physics Letters*, vol. 99, no. 16, p. 162904, 2011.
- [34] E. Bortot and M. Gei, “Harvesting energy with load-driven dielectric elastomer annular membranes deforming out-of-plane,” *Extreme Mechanics Letters*, vol. 5, pp. 62–73, 2015.

- [35] J. B. Shiach, C. G. Mingham, D. M. Ingram, and T. Bruce, “The applicability of the shallow water equations for modelling violent wave overtopping,” *Coastal Engineering*, vol. 51, no. 1, pp. 1–15, 2004.
- [36] T. Todorčević, R. van Kessel, P. Bauer, and J. A. Ferreira, “A modulation strategy for wide voltage output in dab-based dc–dc modular multilevel converter for deep wave energy conversion,” *IEEE Journal of Emerging and Selected Topics in Power Electronics*, vol. 3, no. 4, pp. 1171–1181, 2015.
- [37] B. Holmes, “Tank testing of wave energy conversion systems: marine renewable energy guides,” tech. rep., 2009.
- [38] F. Madsen, L. Yu, P. Mazurek, and A. Skov, “A simple method for reducing inevitable dielectric loss in high-permittivity dielectric elastomers,” *Smart Materials and Structures*, vol. 25, no. 7, p. 075018, 2016.
- [39] G. Moretti, M. Righi, R. Vertechy, and M. Fontana, “Fabrication and test of an inflated circular diaphragm dielectric elastomer generator based on pdms rubber composite,” *Polymers*, vol. 9, no. 7, p. 283, 2017.

ANNEX I: Video analysis of the membrane tip displacement

The time series of CD-DEG’s tip elevation (h) have been reconstructed from the video frames of a high-speed camera, located in front of the wave-flume’s lateral wall, as shown in Figure 10. Knowledge of h is needed to compute the CD-DEG capacitance, C , from Eq. (6). In the following, we describe the video identification procedure used to obtain h .

The elaboration of the high-speed camera frames is achieved through a calibration procedure, aimed at determining the scaling factor to transform the measured height in pixels to the height in millimetres. A two-point calibration is performed using a chessboard with known element side length. Figure 11 shows the two images used for the calibration procedure: the first shows a chessboard far from the camera and the second shows a chessboard close to the camera. The distance between the chessboards in the two images is known and equal to L . Using the width dimensions in pixels (W_1 and W_2) of the two green squares on the chessboard and the real dimension, y , of the green square in millimetres, the following equation provides the scaling factor:

$$s_f = \frac{Ly}{W_1L/2 + W_2L/2}, \quad (24)$$

which results in $s_f = 0.593$ mm/pixel.

After the calibration, the video is filtered using a MATLAB[®] script to identify the exact tip height. The filtering procedure can be divided into the following main steps (see Figure 12):

1. Reading of the i -th frame, I , from the video (coded as `videoObj`).
2. Calculation of the complement image of I .
3. Morphological opening on the grayscale image, I , using a circular sector, F (whose dimensions are small compared to the frame) as structuring element. This function is coded as (`imopen`) and it highlights patterns with the same shape as F within the frame.
4. Conversion of the greyscale image to a binary image, based on the threshold indicated with `alpha`; `alpha` is chosen heuristically.
5. Application of an edge finder filter to the binary image. The “Canny” method has been chosen, which finds the edges by looking for the local maxima of the gradient of I .
6. The value of h is obtained using scaling factor s_f and the height of the tip of the membrane in pixels (h_p): $h = s_f h_p$.

ANNEX II: Validation of the correlation between CD-DEG capacitance and tip elevation

In the calculations presented in Section 5, the CD-DEG capacitance, C , is estimated indirectly from the measured membrane tip displacement, h using Eq. (6). In fact, directly measuring the CD-DEG capacitance while performing energy generation cycles would require a more sophisticated conditioning circuit than that shown in Figure 6a.

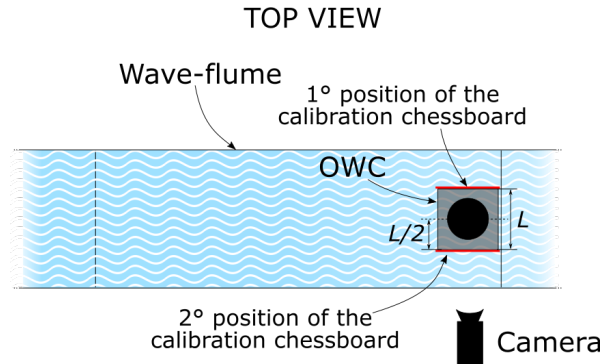


Figure 10: Position of the camera respect to the wave flume.

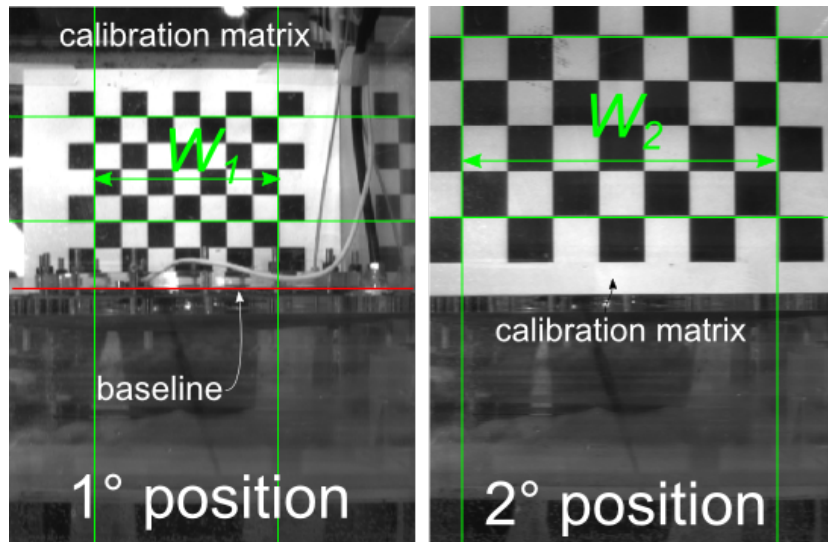


Figure 11: The images used to calibrate the camera.

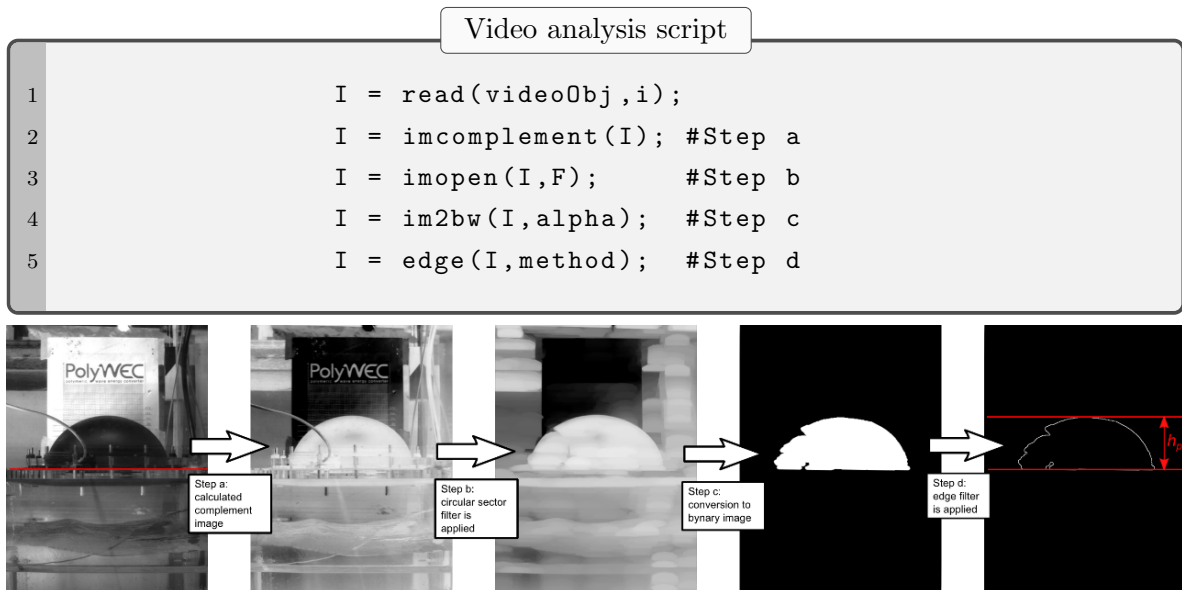


Figure 12: The main steps for the image filtering, with the relative script main phases.

The theoretical correlation between C and h has been validated experimentally through a series of static tests performed with the CD-DEG installed on top of the OWC air chamber and directly connected to the HV power supply.

An external volumetric compressor is connected to the chamber in order to vary its pressurization and induce CD-DEG deformation. A step-wise increase in CD-DEG deformation is realized by prescribing a progressive pressure increase, the CD-DEG tip displacement is measured with a high-speed camera (as in dynamic generation tests), and the associated CD-DEG capacitance at each step is measured by prescribing a high-frequency alternated voltage on its electrodes and measuring its phase shift with respect to the current, as explained in the following.

Capacitance measurement is performed using the circuit shown in Figure 13a. The circuit includes two resistors (with resistance R_A and R_B) in series to the CD-DEG, and a HV power supply. Overall, the system of the CD-DEG and of the two resistors constitutes a R-C dipole. The employed power supply is 10/10B-HS by TREK, which is capable to provide custom voltage profiles. The acquisition electronics are the same described in Section 4.2.

Resistance R_A is 40 k Ω , i.e., comparable to the expected capacitive reactance of the DEG, to produce a significant phase shift between current and voltage over the dipole. Resistance R_B is used to measure the current on the dipole: indicating with V_R the instantaneous voltage on R_B , the current through the dipole is $I = V_R/R_B$. Voltage V_R is acquired through an analogical channel of the conditioning electronics (whose measuring range is ± 10 V), therefore we have chosen $R_B = 1$ k Ω to limit the value of V_R accordingly.

A sinusoidal voltage with amplitude $\Delta V = 200$ V, angular frequency $\omega = 2\pi \cdot 80$ rad/s and bias V_0 is applied on the dipole by the power supply.

For a R-C circuit in steady-state alternated current, the following relation holds between ΔV and the amplitude of the sinusoidal current in the circuit, ΔI :

$$\Delta V = \Delta I \sqrt{R^2 + (\omega C)^{-2}}, \quad (25)$$

where R is the total resistance in the circuit, which is the sum of R_A , R_B , the DEG electrodes resistance and other parasitic resistances in the wires and in the circuit connections, while C is the DEG capacitance in a given configuration. Since electrodes and parasitic resistances are not known a priori, R is unknown, thus it is convenient to introduce a phase angle, φ such that:

$$\sin \varphi = \left(\omega C \sqrt{R^2 + (\omega C)^{-2}} \right)^{-1}. \quad (26)$$

Such an angle represents the phase by which current, ΔI , is delayed with respect to voltage, ΔV , and it can be measured by direct comparison of current and voltage time-series.

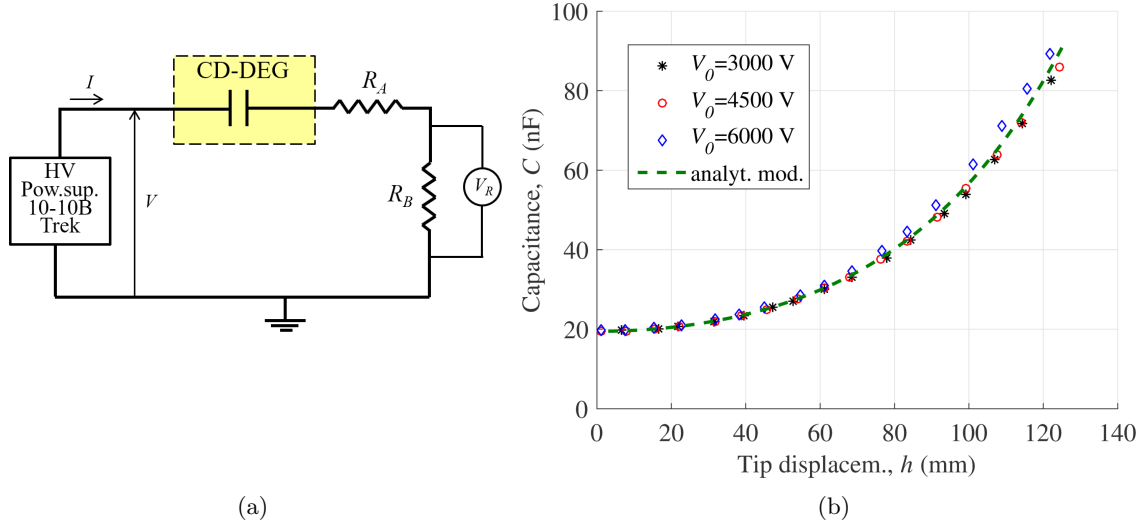


Figure 13: (a) Electrical circuit for the measurement of the CD-DEG capacitance. (b) Measured CD-DEG capacitance at different tip elevation values (h) and applied bias voltages (V_0), and comparison with the analytical model (Eq. (6)).

Using Eqs. (25) and (26), the CD-DEG capacitance at the different intermediate deformations is estimated as follows:

$$C = \frac{\Delta I}{\omega \Delta V \sin \varphi}. \quad (27)$$

Notice that Eq. (27) does not make use of the resistance value of the dipole, which is in fact unknown due to the contribution of the CD-DEG's compliant electrodes.

Tests have been repeated using three different bias voltage values, namely $V_0 = 3000$ V, $V_0 = 4500$ V and $V_0 = 6000$ V i.e., in the same order of the DEG operating voltage, to verify the influence of the applied electrical load on the measured capacitance. Experimental results at different values of V_0 are represented by different markers in Figure 13b. Each experimental point is the result of application of Eq. (27) on sinusoidal current/ voltage signals. Figure 13b also compares the theoretical correlation between h and C (given by Eq. (6)) with experimental data. The good match between the predicted value of C and its experimental measurements at different values of V_0 and h (namely, $|h| < e$) makes it possible to draw the following observations:

1. In practice, the dependence of the measured capacitance on V_0 is very weak, i.e., the capacitance can be expressed as a function of the CD-DEG tip displacement with good approximation.

2. Eq. (6) holds in the observed deformation range, confirming the results observed via finite element simulation in [27].